

Article

Improvement of Treetop Displacement Detection by UAV-LiDAR Point Cloud Normalization: A Novel Method and A Case Study

Kaisen Ma ^{1,2,3} , Chaokui Li ⁴, Fugen Jiang ^{1,2,3} , Liangliang Xu ^{1,2,3}, Jing Yi ^{1,2,3}, Heqin Huang ⁵ and Hua Sun ^{1,2,3,*} 

- ¹ Research Center of Forestry Remote Sensing & Information Engineering, Central South University of Forestry and Technology, Changsha 410004, China; makaisen@csuft.edu.cn (K.M.)
 - ² Key Laboratory of Forestry Remote Sensing Based Big Data & Ecological Security for Hunan Province, Changsha 410004, China
 - ³ Key Laboratory of National Forestry & Grassland Administration on Forest Resources Management and Monitoring in Southern Area, Changsha 410004, China
 - ⁴ National-Local Joint Engineering Laboratory of Geo-Spatial Information Technology, Hunan University of Science and Technology, Xiangtan 411100, China
 - ⁵ Architectural Engineering Institute, Hunan Software Vocational and Technical University, Xiangtan 411100, China
- * Correspondence: sunhua@csuft.edu.cn; Tel.: +86-731-85623450

Abstract: Normalized point clouds (NPCs) derived from unmanned aerial vehicle-light detection and ranging (UAV-LiDAR) data have been applied to extract relevant forest inventory information. However, detecting treetops from topographically normalized LiDAR points is challenging if the trees are located in steep terrain areas. In this study, a novel point cloud normalization method based on the imitated terrain (NPCIT) method was proposed to reduce the effect of vegetation point cloud normalization on crown deformation in regions with high slope gradients, and the ability of the treetop detection displacement model to quantify treetop displacements and tree height changes was improved, although the model did not consider the crown shape or angle. A forest farm in the mountainous region of south-central China was used as the study area, and the sample data showed that the detected treetop displacement increased rapidly in steep areas. With this work, we made an important contribution to theoretical analyses using the treetop detection displacement model with UAV-LiDAR NPCs at three levels: the method, model, and example levels. Our findings contribute to the development of more accurate treetop position identification and tree height parameter extraction methods involving LiDAR data.

Keywords: UAV-LiDAR; forest remote sensing; normalized point cloud; individual tree detection; treetop displacement



Citation: Ma, K.; Li, C.; Jiang, F.; Xu, L.; Yi, J.; Huang, H.; Sun, H. Improvement of Treetop Displacement Detection by UAV-LiDAR Point Cloud Normalization: A Novel Method and A Case Study. *Drones* **2023**, *7*, 262. <https://doi.org/10.3390/drones7040262>

Academic Editors: Tao Cheng, Hengbiao Zheng, Ning Lu and Kai Zhou

Received: 14 March 2023
Revised: 5 April 2023
Accepted: 10 April 2023
Published: 12 April 2023



Copyright: © 2023 by the authors. Licensee MDPI, Basel, Switzerland. This article is an open access article distributed under the terms and conditions of the Creative Commons Attribution (CC BY) license (<https://creativecommons.org/licenses/by/4.0/>).

1. Introduction

Accurate tree height measurements are a core component of forest resource investigations and play an important role in forest management, carbon stock estimations, and ecological effect evaluations [1–3]. Traditional investigation methods have some drawbacks, such as long investigation cycle lengths, poor timeliness, and large manual measurement errors [4–6]. In recent decades, light detection and ranging (LiDAR), an active remote sensing technology, and especially airborne LiDAR scanning based on unmanned aerial vehicle (UAV) platforms have been used to obtain detailed and accurate information on topographic features and forest canopies [7–9]. This advantage is widely used to investigate individual tree parameters, including tree height [10–12], crown area [13–15], and leaf area index [16,17].

Treetop detection is a fundamental and important step in individual tree segmentation and parameter extraction methods based on UAV-LiDAR point clouds and has thus attracted extensive attention [18–20]. Previous studies can be divided into two categories in terms of the data used. One category is based on raster data, including canopy height models (CHMs) and vegetation point cloud density models (VPCDMs). These data are generated based on interpolations of point cloud data and use marker-controlled watershed algorithms or local maxima to explore the locations of treetops [21–23]. The other category is directly based on unstructured point sets, such as normalized point cloud data (NPC); these studies used the spatial structure relationships between the point cloud and the structural characteristics of a forest and methods such as nearest-distance comparisons, regional growth, and threshold judgments, and height thresholding are used [24–26].

Both NPCs and CHMs are representations of objects rising from the terrain that are approximately placed on a plane [27]. However, in forested terrain with complex topography, where local topographic variations cannot be ignored, the above planar terrain assumption is not valid. Previous studies have shown that ignoring topography leads to errors in LiDAR-derived individual tree metrics, such as the derived crown heights and treetop positions, especially for trees with weak crown-top dominance [28,29]. To date, no study has explored a topographic normalization method that can effectively attenuate the errors in normalized point cloud crown deformation data and parameter extraction results.

Therefore, detecting treetops using normalized CHMs and NPCs can be a challenge if the trees are located in areas of complex terrain [30]. These methods are influenced by the differences between the terrain surface and crown features. In treetop detection results obtained through these methods, “false” local maxima may be detected in areas with steeply sloping canopies, and displacement may occur between these maxima and the true treetops. To date, only three previous studies have reported the effects of the above factors on treetop detection considering displacement [31–33]. Khosravipour et al. [31] proposed a theoretical model to quantify the effect of the slope gradient on treetop detection accuracy. In their theoretical model, the horizontal and vertical displacements of the treetops were treated as functions of the slope gradient and crown radius. However, their model is applicable only to trees with spherical canopies. To overcome this limitation, Alexander et al. [32] extended the theoretical model to spherical and conical canopies. Their study showed that the detection error at the treetop was closely related to the slope gradient, crown radius, and crown angle of the conical crown. Later, Nie et al. [33] improved the theoretical treetop displacement model under different topographic conditions. These studies showed that UAV-LiDAR-derived crown point clouds are deformed through topographic normalization. The individually detected trees were displaced under the influence of the crown shape and slope gradient. The current research related to the treetop displacement model has three main deficiencies. (1) The normalized CHMs and NPCs differ from the shape and spatial distribution of the real vegetation scene, resulting in treetop detection displacements. (2) The traditional treetop displacement theoretical model is applicable only for canopies with regular shapes (e.g., spherical, conical, and elliptical). (3) It is difficult to obtain the crown angle parameters required in the traditional treetop displacement theoretical model.

To address these scientific questions, in this paper, we discuss the effects of UAV-LiDAR-derived point cloud topographic normalization on treetop detection displacements in terms of the utilized method, model, and example. Three specific objectives are explored. (1) A novel point cloud normalization method is proposed to reduce the effect of vegetation point cloud normalization on crown deformation in steep terrain. (2) The treetop detection displacement model is improved to more easily quantify treetop movement and tree height change values under the condition of irregular crown shapes. (3) The effects of the above factors are analyzed and validated based on an example of a forest farm in the mountains of south-central China. With this work, we make an important contribution to theoretical analyses of LiDAR point cloud normalization methods and of the treetop detection displacement models. Our results can help researchers develop more accurate treetop location identification and tree height parameter extraction methods using LiDAR data.

2. Materials

2.1. Study Area

Lutou Forest Farm (113.85–113.97° E and 28.52–28.63° N) is located in the Luoxiao Mountains in south-central China (see Figure 1). The area of the farm is 53.08 km², with an elevation of 124 to 1273 m. The terrain is high in the south and low in the north, and the topography mainly includes medium-low mountains. The forest coverage rate is 94.2%, the average temperature is 16.8 °C, and the annual precipitation is approximately 1500 mm. The study area is part of the Lutou Forest Farm, with an area of 0.49 km² and elevations ranging from 250 m to 600 m above sea level. The slope gradient is roughly normally distributed and is mainly concentrated between 30° and 50° (see Figure 2). The forest cover composition predominantly includes Chinese fir (*Cunninghamia lanceolata*), *Cyclobalanopsis glauca* (*Cyclobalanopsis glauca* Thunb. Oerst.), and Bamboo.

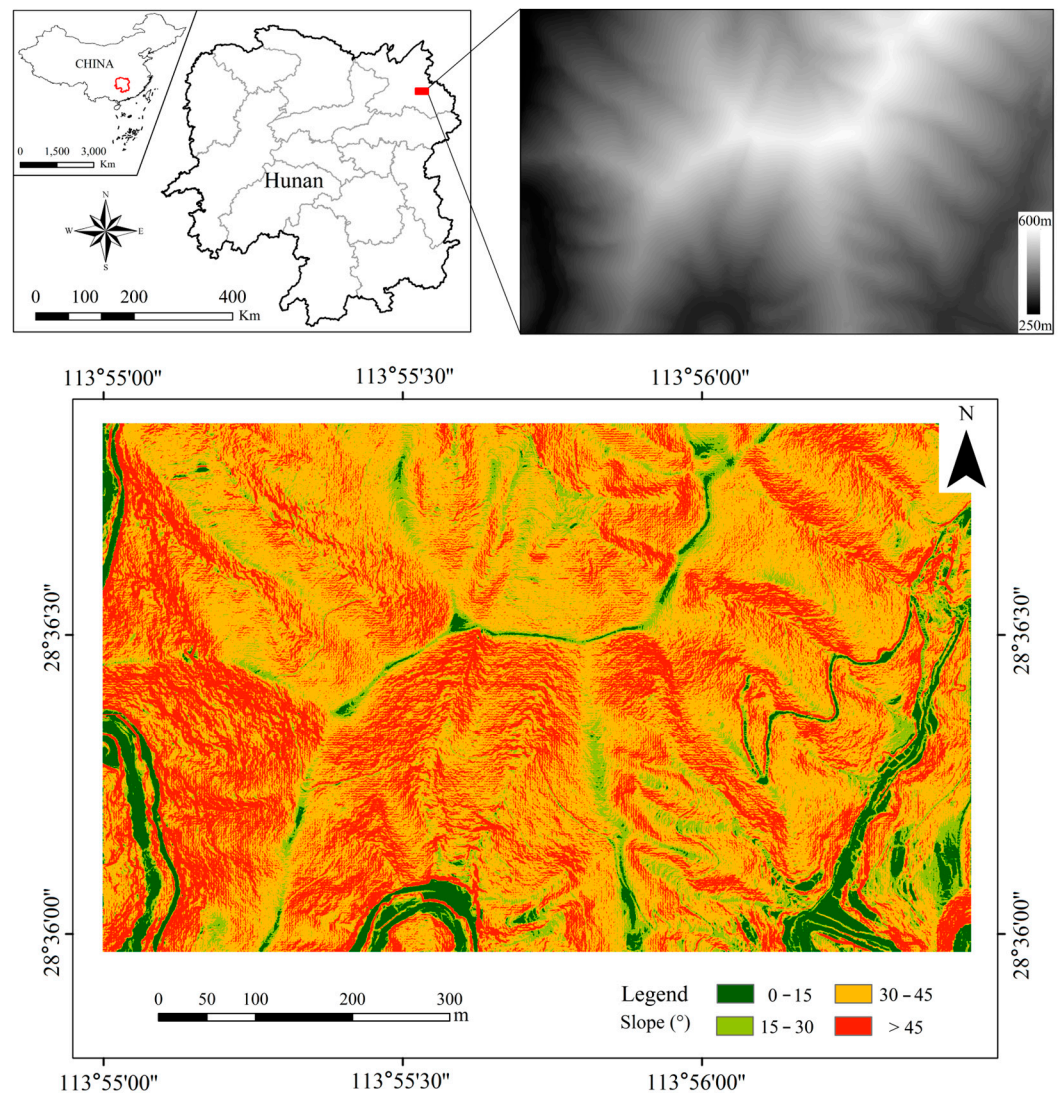


Figure 1. Map of the study area location, including its geographic location, a digital terrain model, and the slope gradient distribution.

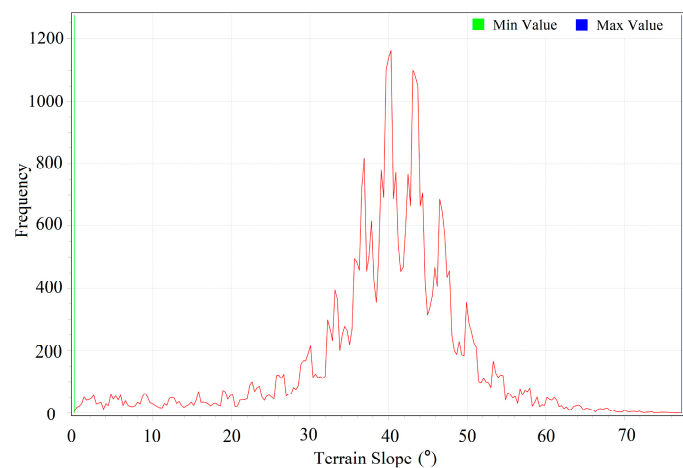


Figure 2. Distribution of the mean slope gradient in the study area.

2.2. LiDAR Data Collection and Preprocessing

The LiDAR point cloud data were acquired in December 2020. The data were obtained using the DJI Matrix 600 UAV platform and a RIEGL VUX-1LR [34]. A vertical intersection route design was adopted for the flight routes. The UAV platform and LiDAR sensor working mode were determined according to the elevation variations and data requirements in the study area. Specifically, the UAV flight speed was 6 m/s, the flight altitude was 100 m above the ground, the flight belt interval was 70 m, the scanning angle of the laser pulse was 140–180°, and the emission frequency was 300 kHz. Then, position and orientation system (POS) processing and aerial belt splicing were performed to obtain the LiDAR point cloud data for the study area. The point cloud density was greater than 500 pts/m² in the ridge region, and the average density was approximately 200 pts/m² in the valley.

The spatial distance-based denoising method was used to remove noisy points caused by leaves, water vapor, etc. The algorithm can determine whether a given point is a noisy point based on the average distance between the target point and all other points in the neighborhood [35].

2.3. Reference Data

Due to the lack of field measurement data representing trees on highly sloping terrain, the height and location information of each individual tree used in the accuracy evaluation was obtained by visual identification. The coordinates from the trunk point cloud were manually depicted in Esri ArcScene[®] software to determine the location of each tree, and the height maximum from the crown point cloud was subtracted from the height minimum of the tree location to obtain the true height of each tree. The integrity of a single tree point cloud is affected by the segmentation algorithm, especially for the tree point cloud with crown intersection and overlap variables. Incomplete canopy point clouds have inherent uncertainties that limit their use in treetop displacement research based on normalization. Trees with distant crowns do not have these problems, and 317 isolated trees were marked in the study area.

3. Methodology

The methodological flowchart of treetop displacement by UAV-LiDAR point cloud normalization research is shown in Figure 3, including a novel normalized point cloud based on imitated terrain method, an improved treetop displacement model, and a tree height accuracy evaluation.

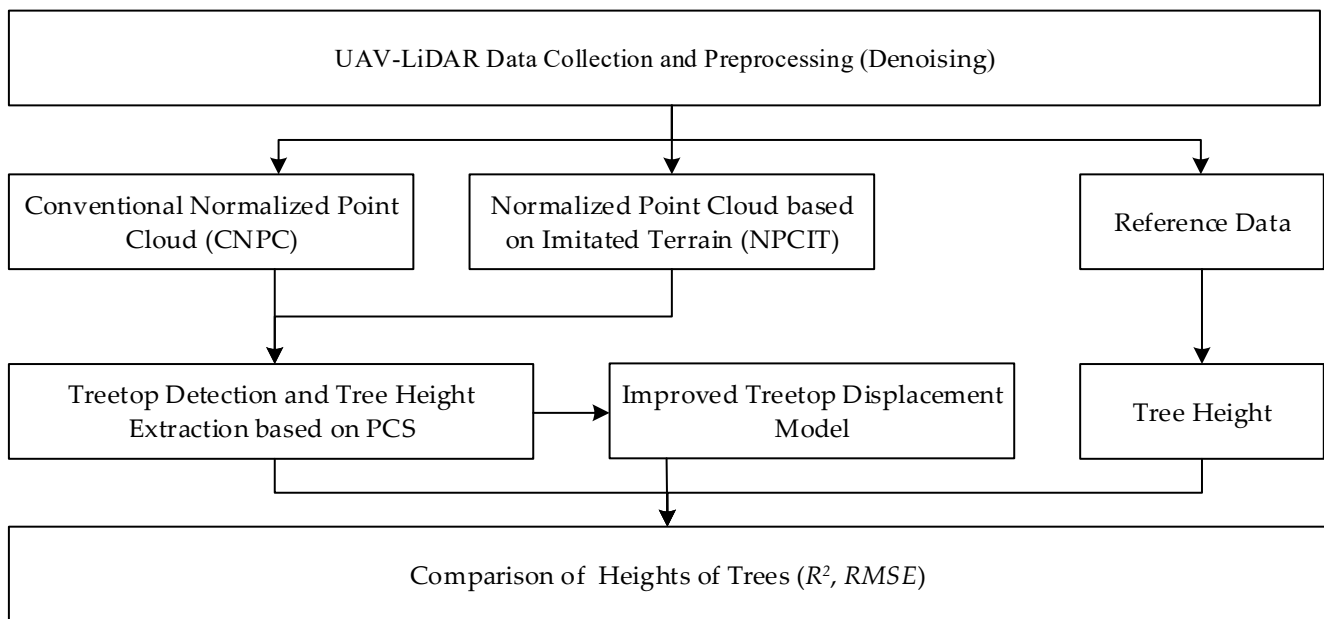


Figure 3. The methodological flowchart of this research.

3.1. Point Cloud Normalization

The conventional normalized point cloud (CNPC) is based on a vertical projection, and the normalized point cloud Z_n is based on the elevation value Z of each surface feature point minus the elevation value Z_0 of the nearest ground point in the vertical space [36]. When point cloud data represent vegetation located in steep-terrain areas, the CNPC method yields a spatial distribution of surface features that is severely compressed, and the error between the point cloud and the real scene becomes very large, leading to crown deformation and reduced forest parameter extraction accuracy. In this study, a novel normalized point cloud based on imitated terrain (NPCIT) was proposed for use in steep-terrain areas. An equidistant projection was established by using the Euclidean distances among the ground point clouds considering local terrain undulations.

A comparison of the characteristics of NPCIT and CNPC is shown in Figure 4. The similarity between these two topographic normalization methods lies in the normalized point cloud height value Z_n , which is the vertical difference (Δz) between surface feature points and ground points. Therefore, the vegetation height parameters extracted using the NPCIT-based normalized point cloud data do not change. The difference is that the distance between the CNPC-based topographic normalization surface feature point clouds is Δx , which is the cosine of the actual distance (l) and the slope gradient. The length L of the whole area is the same as the length before topographic normalization. However, the point cloud plane distance after topographic normalization based on NPCIT is the Euclidean distance (l) between the adjacent ground points in the real scene, and the length L' of the whole region becomes larger than the original length L .

In the CNPC method using vertical projection, the size of the grids before and after normalization is the projected area of the plane. The data for the entire study area are arranged neatly and tightly based on a grid approach. In this study, the NPCIT-based topographic normalization stretched the field point cloud data by imitating the undulations of the terrain, and the algorithm consisted of constructed triangular meshes, isometric transformed meshes, an equidistant conversion of point clouds within the meshes, a normalization step, and an algorithm implementation step. The side length of the triangular meshes based on NPCIT varied with terrain relief and the converted adjacent grids may have been influenced by local stacking or gaps. Therefore, the main difficulties faced when using this method involved controlling the extent of stretching and ensuring the integrity of the data during the normalization process. The specific concept is described as follows.

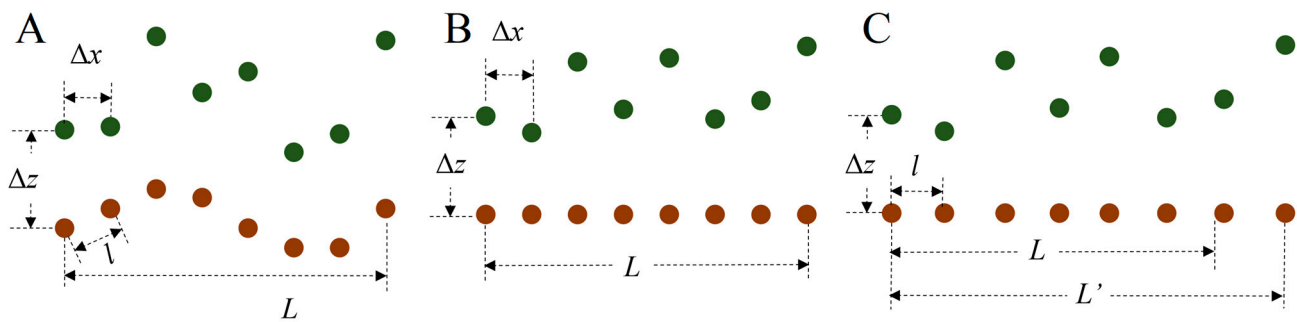


Figure 4. Simplified topographic normalization principles of various point cloud normalization methods: an original LiDAR-derived point cloud (A), a point cloud normalized based on a CNPC (B), and a point cloud for NPCIT (C).

3.1.1. Triangular Mesh Construction

The direct normalization of an overall UAV-LiDAR point cloud region based on NPCIT leads to a large deformations value and data gaps in the study area due to the influence of topographic relief. Therefore, it was necessary to delineate the entire study area according to triangular meshes composed of ground points. The method by which these triangular meshes were constructed is described as follows:

(1) Ground point classification. We used an improved progressive triangular irregular network (TIN) identification (IPTD) method to separate the ground points [37,38]. This algorithm generates a sparse triangulated irregular network through seed points and encrypts each layer through iterative processing until all of the ground points are classified. The key parameters of the algorithm include the iteration distance, iteration angle, and maximum slope gradient; in this study, these parameters were set to 0.5 m, 5° , and 70° , respectively.

(2) Resampling of ground points. To ensure that the meshes used for partitioning are similar in size and optimally evenly distributed, it is necessary to resample the classified ground point cloud data. We selected the minimum point spacing method for resampling. When the minimum point spacing was set to n , only one point within each radius size of n was selected.

(3) Building meshes. The resampled ground points were used to construct an irregular triangular network. The whole study area was divided into numerous triangular regions, and each region was normalized based on NPCIT to reduce the deformation degree.

3.1.2. Isometric Mesh Transformation

The isometric transformation process for the mesh in this study involved the isometric transformation of triangular meshes by imitating the Euclidian distances between terrains. First, it was necessary to select a suitable initiation point in the whole research area to identify the first transformed mesh. We selected the ground point with the largest elevation near the center point of the study area as the initiation point. Then, according to the relevant adjacency relationships, other triangular meshes were transformed in turn. The three-dimensional distance between the meshes before the isometric transformation was equal to the planar distance after the mesh transformation. Stretching was performed from the perspective of planar projection, but the actual lengths were equal. The isometrically transformed triangle meshes are shown in Figure 5. The light blue triangles are the original meshes, and the light green triangles are the transformed meshes. According to the mesh vertex type, the isometric transformation of the triangular network was divided into three cases.

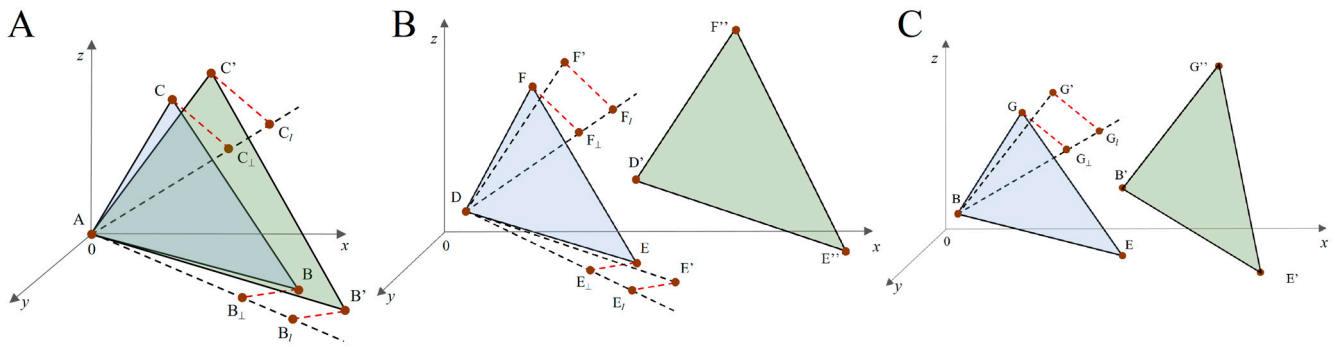


Figure 5. Three cases of isometric mesh transformation: Case 1 (A), Case 2 (B), and Case 3 (C).

Case 1: One point in the triangular mesh is used as the initiation point, as shown in Figure 5A. In $\triangle ABC$, A is the initiation point, and B and C are the points to be transformed. For example, consider the transformation of point B to point B'. The vertical point B_{\perp} is obtained in the xoy plane, and $OB_{\perp} \perp BB_{\perp}$; B_l is a point on the extension of AB_{\perp} , and $AB_l = AB$; B' is the point vertically above B_l , and $BB_{\perp} = B'B_l$. If A, B, and C are expressed as (x_A, y_A, z_A) , (x_B, y_B, z_B) , and (x_C, y_C, z_C) , respectively, the three vertices $A'(x_{A'}, y_{A'}, z_{A'})$, $B'(x_{B'}, y_{B'}, z_{B'})$, and $C'(x_{C'}, y_{C'}, z_{C'})$ of the transformed triangular mesh satisfy the following relations:

$$L_{AB} = \sqrt{(x_A - x_B)^2 + (y_A - y_B)^2 + (z_A - z_B)^2} \tag{1}$$

$$L_{AB_{\perp}} = \sqrt{(x_A - x_B)^2 + (y_A - y_B)^2} \tag{2}$$

$$\frac{|x_B - x_A|}{L_{AB_{\perp}}} = \frac{|x_{B'} - x_A|}{L_{AB}} \tag{3}$$

$$x_{B'} = \frac{(x_B - x_A) \times L_{AB}}{L_{AB_{\perp}}} = \frac{|x_B - x_A| \times \sqrt{(x_A - x_B)^2 + (y_A - y_B)^2 + (z_A - z_B)^2}}{\sqrt{(x_A - x_B)^2 + (y_A - y_B)^2}} \tag{4}$$

$$y_{B'} = \frac{|x_{B'} - x_A| \times |y_B - y_A|}{|x_B - x_A|} \tag{5}$$

$$z_{B'} = z_B \tag{6}$$

Case 2: One vertex is transformed, and the other two points are to be transformed. As shown in Figure 5B, in $\triangle DEF$, point D is transformed to D', and E and F are the points to be transformed. First, E and F are transformed into E' and F' according to the rules in Case 1, and then $\triangle DE'F'$ is translated to $\triangle D''E''F''$ by using the relationship between D' and D. If points D, E, and F are expressed as (x_D, y_D, z_D) , (x_E, y_E, z_E) and (x_F, y_F, z_F) , respectively, the three vertices $D'(x_{D'}, y_{D'}, z_{D'})$, $E''(x_{E''}, y_{E''}, z_{E''})$, and $F''(x_{F''}, y_{F''}, z_{F''})$ of the transformed triangular mesh satisfy the following relations:

$$x_{E'} = \frac{(x_E - x_D) \times L_{DE}}{L_{DE_{\perp}}} = \frac{(x_E - x_D) \times \sqrt{(x_E - x_D)^2 + (y_E - y_D)^2 + (z_E - z_D)^2}}{\sqrt{(x_E - x_D)^2 + (y_E - y_D)^2}} \tag{7}$$

$$y_{E'} = \frac{|x_{E'} - x_D| \times |y_E - y_D|}{|x_E - x_D|} \tag{8}$$

$$z_{E'} = z_E \tag{9}$$

$$L_{DD'} = \sqrt{(x_{D'} - x_D)^2 + (y_{D'} - y_D)^2 + (z_{D'} - z_D)^2} \quad (10)$$

$$x_{E''} = x_{E'} + |x_{D'} - x_D| \quad (11)$$

$$y_{E''} = y_{E'} + |y_{D'} - y_D| \quad (12)$$

$$z_{E''} = z_E + |z_{D'} - z_D| \quad (13)$$

Case 3: Two vertices of the triangle mesh are transformed, and the other point needs to be transformed, as shown in Figure 5C. In $\triangle BEG$, points B and E are transformed into B' and E', and the transformation of G to G'' is the same as that for point E in Case 2.

3.1.3. Equidistant Conversion of Point Clouds within the Meshes

The triangular meshes were isometrically transformed in Step 2, but the other ground and vegetation point clouds inside each triangular mesh were not transformed. We chose to convert the point clouds by using the equidistant relationships between the points inside the triangles and the triangle boundaries, as shown in Figure 6. In $\triangle ABC$ and the transformed $\triangle A'B'C'$, the points can be expressed as follows: A(x_A, y_A, z_A), B(x_B, y_B, z_B), C(x_C, y_C, z_C), A'($x_{A'}, y_{A'}, z_{A'}$), B'($x_{B'}, y_{B'}, z_{B'}$), and C'($x_{C'}, y_{C'}, z_{C'}$). With point P(x_P, y_P, z_P) as an example, the extension of the line AP (Equation (16)) intersects the line BC (Equation (17)) at Q(x_Q, y_Q, z_Q) (Equations (18) and (19)). The equidistance among points P, P', Q, and Q' in the two meshes before and after the conversion is shown in (Equations (20) and (21)). These calculations are repeated for the other point clouds until all points in the meshes are converted.

$$k_{AP} = \frac{y_A - y_P}{x_A - x_P} \quad (14)$$

$$k_{BC} = \frac{y_B - y_C}{x_B - x_C} \quad (15)$$

$$AP = y_A - \frac{y_A - y_P}{x_A - x_P} \times x_A \quad (16)$$

$$BC = y_B - \frac{y_B - y_C}{x_B - x_C} \times x_B \quad (17)$$

$$x_Q = \frac{BC - AP}{k_{AP} - k_{BC}} \quad (18)$$

$$y_Q = k_{AP} \times x_Q + AP \quad (19)$$

$$\frac{BQ}{QC} = \frac{B'Q'}{Q'C'} \quad (20)$$

$$\frac{AP}{PQ} = \frac{A'P'}{P'Q'} \quad (21)$$

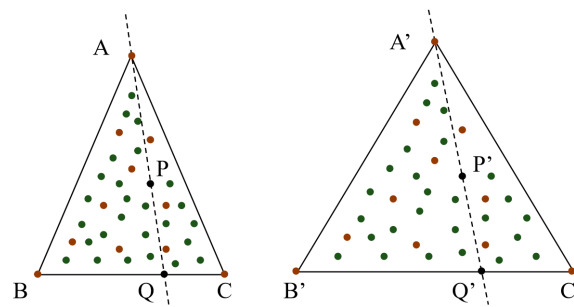


Figure 6. Schematic diagram of the equidistant conversion of point clouds within the meshes.

3.1.4. Normalization

Through the above process, a complete imitated terrain conversion of the point cloud is achieved, where the converted cloud points x and y are changed and the z values retain the original heights (Equations (6) and (9)). The normalized values are generated by subtracting the ground elevation, Z_0 , from the original sea level height, Z_x , of the point cloud (Equation (22)).

$$Z_n = Z_x - Z_0 \quad (22)$$

3.1.5. Algorithm Implementation

The novel normalized point cloud methods proposed in this study were run and implemented on PyCharm Community Edition 2021.3.1 using the Python programming language, wherein the math module and the OS module were used for the mathematical mesh operations and the point cloud conversion within the mesh, respectively, and the OS module was used for the sequential reading of the partitioned point cloud folder files. The math module was used to perform the mathematical point cloud conversion operation within the grid, and the os module was used for the sequential reading of the partitioned point cloud folders. The core code is openly available at https://github.com/csuft-mks/py_NPCIT (accessed on 14 March 2023).

3.2. Theoretical Model of Treetop Displacement

The treetop displacement model was used to simulate and quantify the influence of the slope gradient and crown shape on the treetop detection results in both the vertical direction (change in the tree height value) and the horizontal direction (shift in position). The treetops detected using the normalized point cloud were displaced due to the slope of the terrain. As shown in Figure 7, Point A in the original point cloud is a treetop, and the normalized point cloud detects Point B. There is thus a displacement between the two points.

3.2.1. Original Model

Kosravipur et al. [31] and Alexander et al. [32] proposed theoretical treetop displacement models that are applicable to conical and spherical tree crown structures, respectively, and can be used to quantify treetop detection accuracy. Nie et al. [33] extended this approach to scenes with different terrain changes. As shown in Figure 8, taking a conical crown on inclined terrain as an example, in their models, the slope gradient is denoted as α , the crown radius is R , the crown angle is β , the tree height is H , the branch height is H_u , the horizontal displacement is ΔL , and the vertical displacement is ΔH .

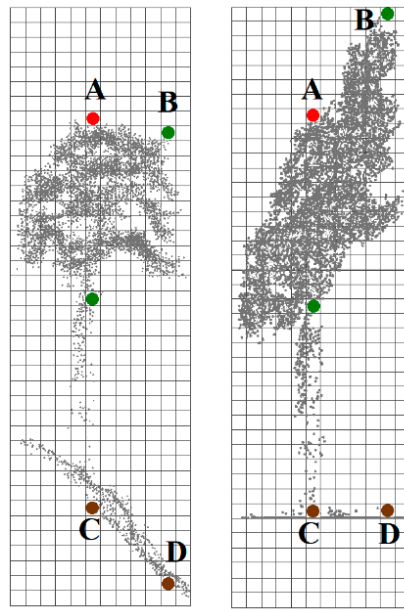


Figure 7. Schematic diagram showing a comparison between the original and normalized point clouds containing individual trees located in high-gradient terrain. The lengths of AC and BD in the figure are unchanged.

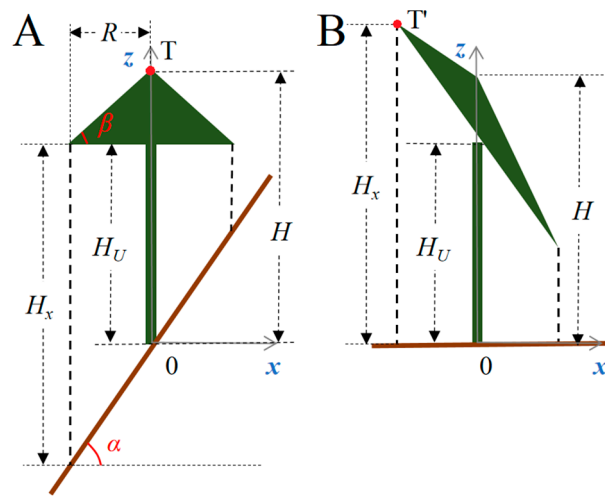


Figure 8. Schematic diagram of the theoretical treetop displacement model. In the tree model with the original point cloud (A), the treetop reaches a maximum value T at the center of the crown. In the tree model with the normalized point cloud (B), the treetop T' is displaced to the left.

When the crown angle is greater than the slope gradient ($\beta > \alpha$), the treetop point cloud is higher than all other crown points before and after topographic normalization, and the detected treetops do not change. However, when β is less than α , treetop displacement occurs; in this situation, the horizontal displacement ΔL is equal to the horizontal distance between the point of the height maximum value and the real treetop, and the maximum distance is the crown radius (Equation (27)), so the vertical displacement ΔH is related to α , β , and R as follows (Equation (25)):

$$H_x = H_U + x \tan \alpha \tag{23}$$

$$H = H_U + x \tan \beta \tag{24}$$

$$\Delta H = H_x - H = H_U + x \tan \alpha - (H_U + x \tan \beta) = x(\tan \alpha - \tan \beta) \tag{25}$$

$$\Delta L_{max} = R \tag{26}$$

$$\Delta H_{max} = R(\tan \alpha - \tan \beta) \tag{27}$$

3.2.2. Improved Model

There are two obvious shortcomings in the original model: a. The model is applicable only to trees with regularly shaped tree crown structures, and b. It is difficult to obtain the crown angle, β , required to calculate vertical displacement. Therefore, we proposed an improved treetop displacement model (see Figure 9) that does not depend on the crown structure. The specific concept of this model is described as follows:

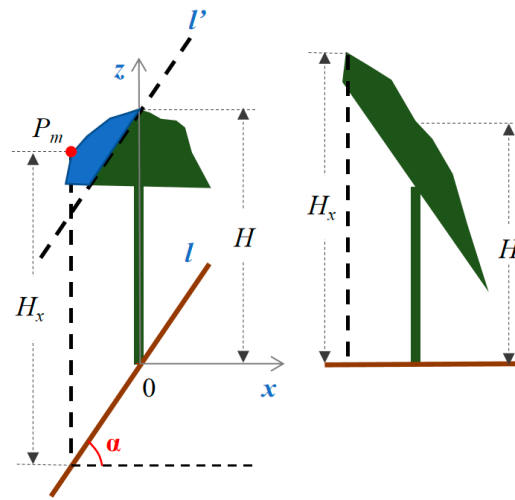


Figure 9. Schematic diagram of the improved treetop displacement model. The blue area is the crown area that causes the treetop to be displaced, and the red dot is the location of the “false” treetop.

(1) Determine the potential tree crown displacement area

The lowest tree point is considered the coordinate axis origin, 0, the horizontal direction is the x-axis, and the vertical direction is the z-axis. The linear function, l (Equation (28)), is constructed with the tangent of the slope gradient, and l is translated upwards to the treetop position to obtain l' (Equation (29)). Then, the point set P_i (the blue area in Figure 9), above the linear function l' , is the crown area that may cause the detection displacement of the treetop. Defining this area as $P_i(x_i, y_i, z_i)$, the z_i values of all points satisfy Equation (30).

$$l : z = x \tan \alpha \tag{28}$$

$$l' : z = x \tan \alpha + H \tag{29}$$

$$z_i > x \tan \alpha + H \tag{30}$$

(2) Confirmation of a “false” treetop position

In the point set P_i , the vertical distance from each point to the linear function, l' , is $dist$. When the distance of point $P_m(x_m, y_m, z_m)$ is $dist_{max}$, P_m is the position of the “false” treetop detected by the normalized point cloud (the red point in Figure 9).

(3) Quantified displacement

Using the relationship between x_m and z_m at point P_m and the origin of the coordinate system, the ΔL displacement (Equation (31)), ΔH displacement (Equation (32)), and height H_x (Equation (33)) of the “false” treetop after detection can be directly obtained.

$$\Delta L = x_m \tag{31}$$

$$\Delta H = dist_{max} = z_m - (x_m \tan \alpha + H) \tag{32}$$

$$H_x = \Delta H + H = z_m - x_m \tan \alpha \tag{33}$$

In the improved treetop displacement model, the potential displacement of the tree crown area and the “false” treetop position are judged directly according to the terrain conditions. The variables used to quantify treetop displacement include the slope gradient α , x_m , y_m , and the tree height H . Compared to the original treetop displacement model, the improved model is applicable to all tree crown structures, and the variables in the model are easy to obtain.

3.2.3. Treetop Displacement Comparison between CNPC and NPCIT

To explore the improved performance of the NPCIT method proposed in this study based on the treetop detection displacement, we compared the two datasets constructed based on the CNPC and NPCIT methods in the improved treetop displacement model. In Figure 10, Figure 10A shows the original tree point cloud dataset, and Figure 10B shows the tree point cloud dataset after the conversion based on the imitated terrain. The slope gradients of these two datasets are α and β , and their tangent values are $\tan \alpha$ (Equation (35)) and $\tan \beta$ (Equation (38)).

$$a^2 + b^2 = c^2 \tag{34}$$

$$\tan \alpha = \frac{b}{a} \tag{35}$$

$$b = a \tan \alpha \tag{36}$$

$$c^2 + b^2 = d^2 \tag{37}$$

$$\tan \beta = \frac{b}{c} = \frac{b}{\sqrt{a^2 + b^2}} = \frac{a \tan \alpha}{\sqrt{a^2 + a^2 \tan^2 \alpha}} = \frac{\tan \alpha}{\sqrt{1 + \tan^2 \alpha}} \tag{38}$$

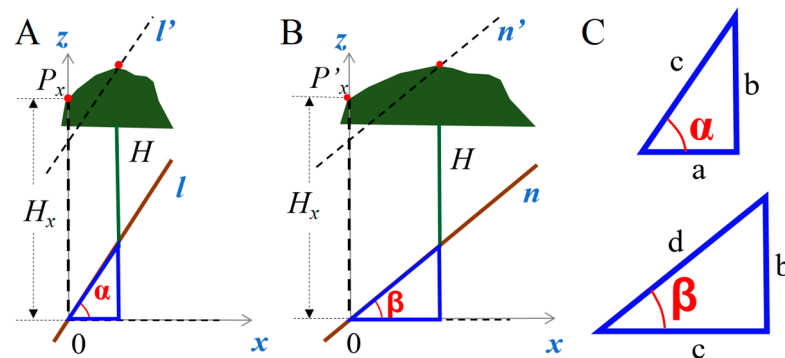


Figure 10. Comparison of the CNPC-based and NPCIT-based treetop displacement schemes. (A) is the original point cloud tree model, (B) is the tree model after imitating the terrain transformation, and (C) is the relationship between the terrain slope angles from the two data models.

After the topographic normalization of dataset A, the vertical displacement ΔH (Equation (32)) and tree height H_x (Equation (33)) are determined. In dataset B, the vertical displacement $\Delta H'$ (Equation (39)) and tree height H_x' (Equation (40)) are obtained with the improvement value ω (Equation (41)) between dataset A and dataset B.

$$\Delta H' = z'_m - (x'_m \tan \beta + H) \tag{39}$$

$$H'_x = z'_m - x'_m \tan \beta \tag{40}$$

$$\omega = \Delta H' - \Delta H = z'_m - (x'_m \tan \beta + H) - [z_m - (x_m \tan \alpha + H)] \tag{41}$$

Based on x_m and z_m , and the converted values x'_m and z'_m , and by combining Equations (38) and (40), the final improvement value ω (Equation (43)) can be simplified. The relationship between the improvement value ω and slope gradient α is shown in Figure 11 for a constant x_m value of 1. The steeper the terrain is, the greater the improved vertical displacement value of the NPCIT method is.

$$H'_x = z'_m - (x'_m \tan \beta) = z_m - \frac{x_m \tan \alpha}{\sqrt{1 + \tan^2 \alpha}} \tag{42}$$

$$\omega = \Delta H' - \Delta H = x_m \tan \alpha \left(1 - \frac{1}{\sqrt{1 + \tan^2 \alpha}}\right) \tag{43}$$

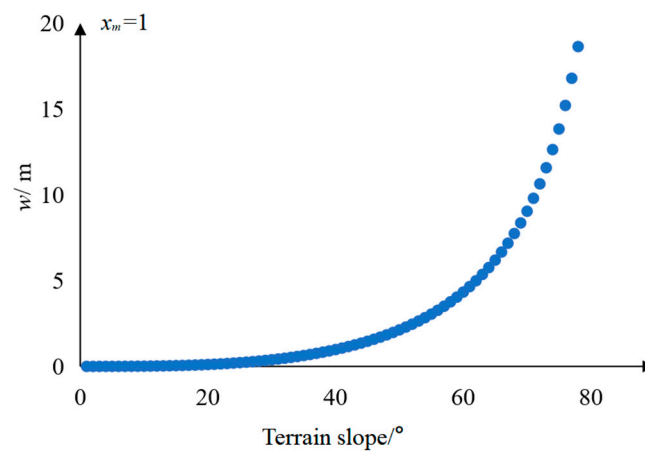


Figure 11. Statistics of the improved vertical displacement of the NPC, based on the NPCIT method, compared to the CNPC method for treetop detection.

3.3. Treetop Detection and Tree Height Extraction

The point cloud segmentation (PCS) algorithm combines region-growing and thresholding judgment steps to segment individual tree point clouds from the normalized clouds [18]. The algorithm mainly considers that there is a certain Euclidean distance between two trees in a tree point cloud, especially between the tops of trees. It is assumed that the highest point in a tree point cloud is the tree apex, and the tree apex can be used as a seed point to establish the growing corresponding region and separate individual trees; this process is iterative [39]. Each segmentation step involves growing the region from the treetop to the ground surface and determining the distance threshold. The height maximum of the isolated normalized individual tree point cloud is the height of the tree. The difference between the X-Y coordinates in treetop detection and in the real treetop location is the horizontal displacement in the treetop displacement model.

3.4. Comparison of the Locations and Heights of Trees

We evaluate the tree height H_x detected in the NPC based on the PCS method using the height H_i of the tree in the reference data as the true value. The accuracy of the detected tree height is evaluated using the coefficient of determination R^2 (Equation (44)) and the root mean square error (RMSE) (Equation (45)); then, the difference between the detected tree height and reference tree height is used to represent the displacement of the treetop in the vertical direction, ΔH (Equation (46)) [40].

$$R^2 = \frac{\sum_{i=1}^n (H_i - \overline{H_i})(H_x - \overline{H_x})}{\sqrt{\sum_{i=1}^n (H_i - \overline{H_i})^2 \sum_{x=1}^n (H_x - \overline{H_x})^2}} \tag{44}$$

$$RMSE = \sqrt{\frac{\sum_{x=1}^n (H_x - H_i)^2}{n}} \quad (45)$$

$$\Delta H = H_x - H_i \quad (46)$$

4. Results

4.1. Topographic Normalization Based on the NPCIT Method

In this study, we performed topographic normalization based on the NPCIT method for the whole study area, obtained normalized vegetation point cloud data, and compared the results with those obtained using the CNPC method. We selected the highest terrain point (113.66 E, 28.61 N, and 564.91 m) in the central part of the whole study area as the initiation point, and the minimum ground point resampling spacing was set to 20 m. In Figure 12, Figure 12A shows the original point cloud data of the whole research area, Figure 12B shows the point cloud data converted based on imitated terrain, Figure 12C shows the NPC derived based on the CNPC method, and Figure 12D shows the NPC obtained based on the NPCIT method. From a visual comparison, the terrain variation and surface height information for the point cloud based on the imitated terrain in the study area can be seen to be consistent with the characteristics of the original point cloud. The terrain is low on the left side, and there is a ridge to the northeast direction of the centre of the area. The difference between the results is that the area of the NPC derived based using the NPCIT method is expanded. The original point cloud area was 0.49 km², while the area of the point cloud obtained with the imitated terrain conversion was approximately 0.53 km².

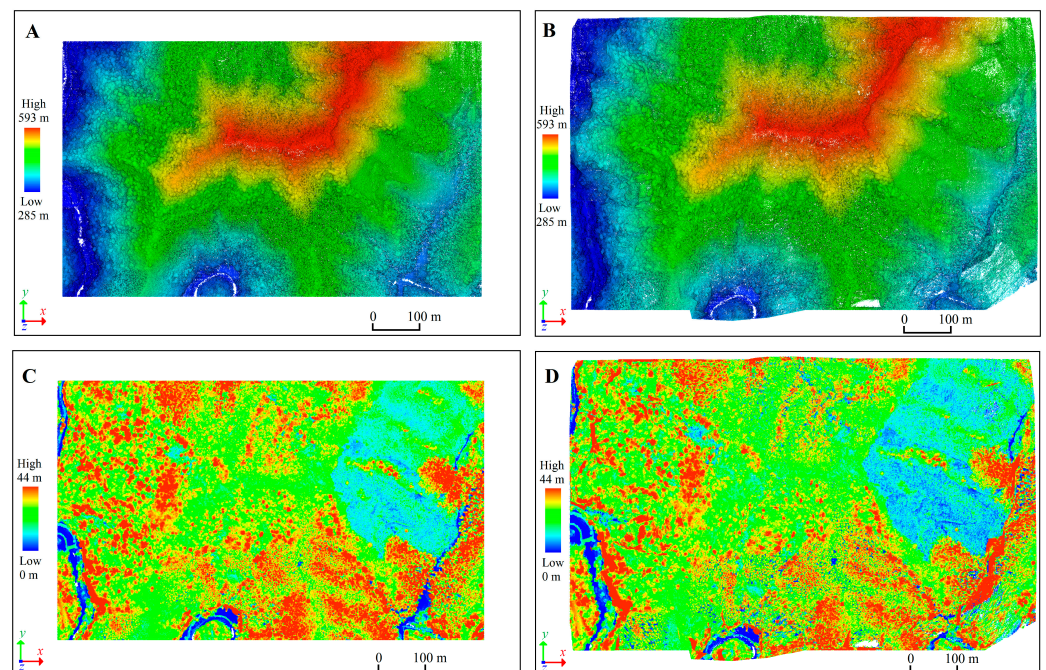


Figure 12. Point clouds representing the study area. (A) is the original point cloud of the study area, (B) is the point cloud after the imitated terrain conversion, (C) is the NPC derived based on the CNPC method, and (D) is the NPC derived based on the NPCIT method.

In addition, the undulation of the terrain displays decreased relief; the original terrain is comparatively steeper, and the relief of the obtained terrain is moderate. We counted the areas of the four mesh categories with slope gradients of 20°, 30°, 40°, and 50° before and after the imitated terrain conversion, as shown in Figure 13.

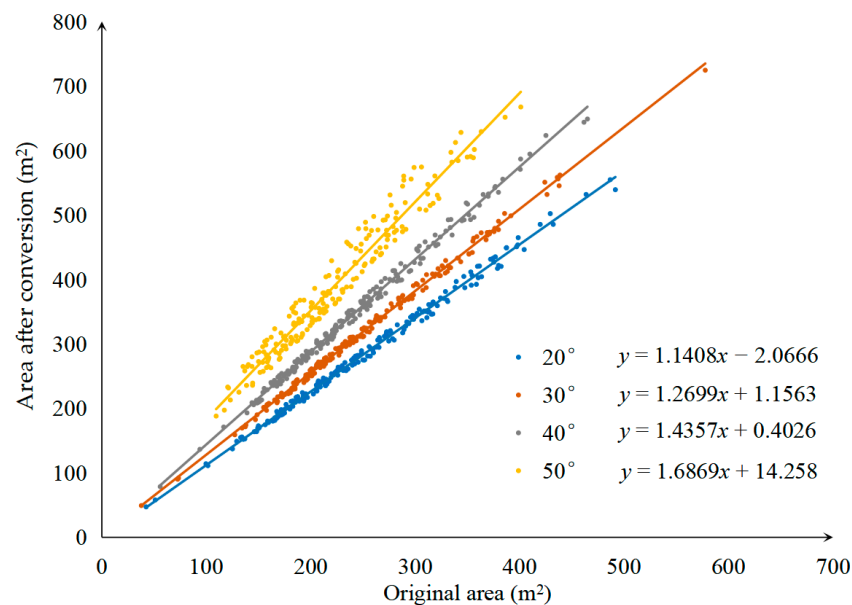


Figure 13. Statistical plot comparing the original area of the mesh with the area following conversion under four slope gradient conditions.

When the slope gradient of the mesh is 20°, the slope of the linear regression is 1.1408, and the area after conversion basically does not change. When the slope gradient of the mesh is 50°, the slope of the linear regression is 1.6869, and the area changes significantly following the conversion. As the slope gradient of the mesh increases, the slope of the linear regression between the original and transformed areas of the same mesh class also increases. Therefore, during the conversion of the imitated terrain features, the smaller the slope gradient of the mesh is, the smaller the change in the converted area. The greater the slope gradient of the mesh is, the greater the areal change after the conversion.

Specifically, in Figure 14, Figure 14A shows the results obtained for an area with a terrain slope of 45°, where four isolated trees grow. Figure 14B shows the NPC derived based on the CNPC method. The crown point cloud of the four trees has undergone obvious deformation, and the “false” treetop has moved toward the low-slope-gradient direction. The distance, L , among the four trees is 50 m, which is the same as the horizontal distance in the original point cloud. Figure 14C shows the NPC derived based on the NPCIT method. From a visual perspective, mesh stretching causes the length of the region to grow from L to L' , and the rearrangement of the crown point cloud mainly manifests as stretching. The crowns of these four trees are similar to those in the original point cloud and are not deformed. The treetop positions are located near the trunks. The distance, L' , among the four trees is 71 m, which is the same as the Euclidean distance obtained from the original point cloud. The experimental results show that compared to the CNPC-based NPC, the NPC obtained based on the NPCIT method exhibits significantly weakened crown deformation, and the arrangement distances of the trees are closer to the real distances.

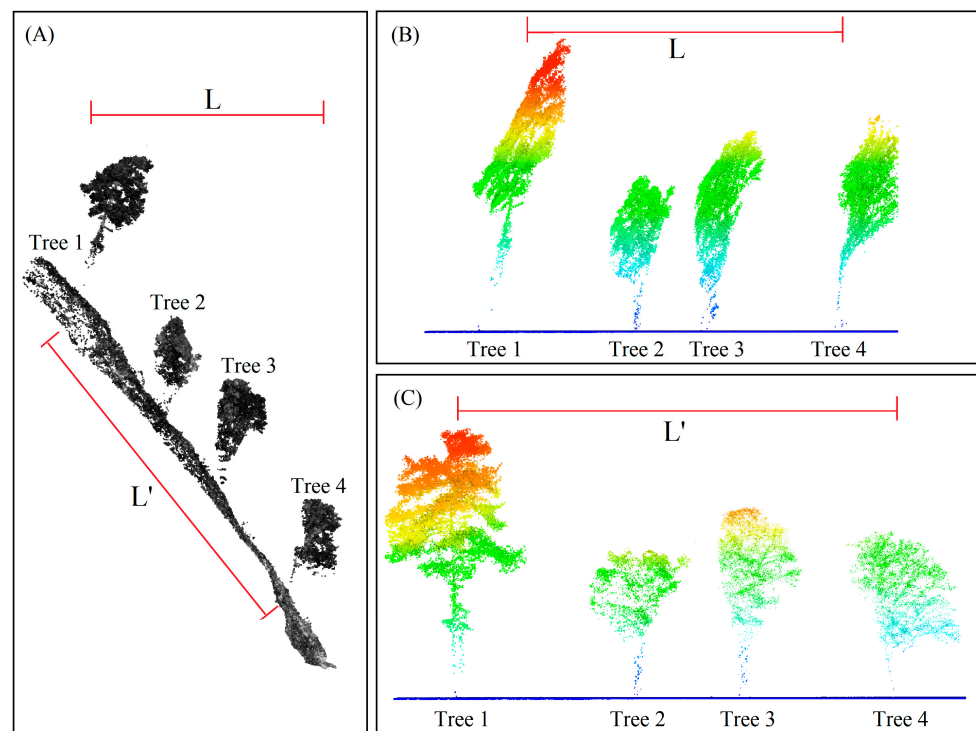


Figure 14. Detailed comparison of trees in the NPCs obtained for steep terrain. (A) Point cloud of the original scene, (B) NPC derived based on the CNPC method, and (C) NPC derived based on the NPCIT method.

4.2. Influence of the Slope Gradient on Treetop Detection Displacement

To verify the proposed treetop displacement theoretical model with examples, we selected the point cloud data for 317 isolated trees without overlapping crowns in the study area as reference data and performed topographic normalization based on the CNPC and NPCIT methods. The numbers and percentages of trees with horizontal and vertical displacements in the treetop detection results obtained from these two NPC datasets are shown in Table 1. The detection results of the NPC data obtained based on the CNPC method show that when the slope gradient was less than 20° , only 4 (3.7%) of the 108 trees underwent treetop displacement, with an average horizontal displacement of 2.78 m and an average vertical displacement of 0.21 m. Among the 62 trees identified on slope gradients greater than 50° , all of the detected treetops were displaced, with an average displacement of 3.27 m and an average vertical displacement of 4.48 m. However, due to the terrain stretching in the NPC data derived based on the NPCIT method, the normalized terrain undulation was reduced. When the original slope gradient of the data is greater than 35° , detected treetop displacement may occur. The results show that as the slope gradient increased, the probability of treetop detection displacement increased. Compared to the NPC obtained based on CNPC, the treetop detection displacement results derived based on the NPCIT method showed obvious improvement.

A total of 144 individual trees detected based on the PCS method experienced displacement, and we analyzed the relationship between the vertical-direction displacement and the slope gradient; the results are shown in Figure 15. In the NPC derived based on CNPC, $R^2 = 0.886$ and $RMSE = 3.433$ m (see Figure 15A) between the reference and measured tree heights. The vertical-direction displacement of the treetops increased rapidly with an increasing slope gradient (see Figure 15B), exceeding 8 m for individual trees at a slope gradient of approximately 60° . However, in the NPC based on the NPCIT method, $R^2 = 0.98$ and $RMSE = 0.298$ m between the reference and measured tree heights (see Figure 15C). Only 32 trees experienced vertical treetop displacement, and these trees were mainly concentrated in steep areas with slope gradients greater than 35° (see Figure 15D).

All of the errors were tree height overestimations, something that was in accordance with the principle of the treetop displacement detection model.

Table 1. Percentages and numbers of correctly detected trees located on slopes with three different gradients.

| Slope Class (°) | Number of Trees | CNPC-Detected Treetops with Displacement | | | | | | NPCIT-Detected Treetops with Displacement | | | | | | | |
|-----------------|-----------------|--|----------------|-----|------|--------------|------|---|-----------|----------------|-----|------|--------------|------|------|
| | | n (%) | Horizontal (m) | | | Vertical (m) | | | n (%) | Horizontal (m) | | | Vertical (m) | | |
| | | | Min | Max | Mean | Min | Max | Mean | | Min | Max | Mean | Min | Max | Mean |
| <20 | 108 | 4 (3.7) | 1.3 | 3.4 | 2.78 | 0.04 | 0.4 | 0.21 | 0 | - | - | - | - | - | - |
| 20–34 | 78 | 31 (39.7) | 1.6 | 4.5 | 2.94 | 0.01 | 2.21 | 0.87 | 0 | - | - | - | - | - | - |
| 35–49 | 69 | 47 (68.1) | 0.9 | 4.5 | 2.78 | 0.11 | 4.06 | 1.43 | 7 (10.1) | 0.9 | 2.4 | 1.66 | 0.12 | 0.48 | 0.27 |
| >50 | 62 | 62 (100) | 1.1 | 5.2 | 3.27 | 0.31 | 8.62 | 4.48 | 25 (40.3) | 1.3 | 5.2 | 2.96 | 0.03 | 1.63 | 0.73 |

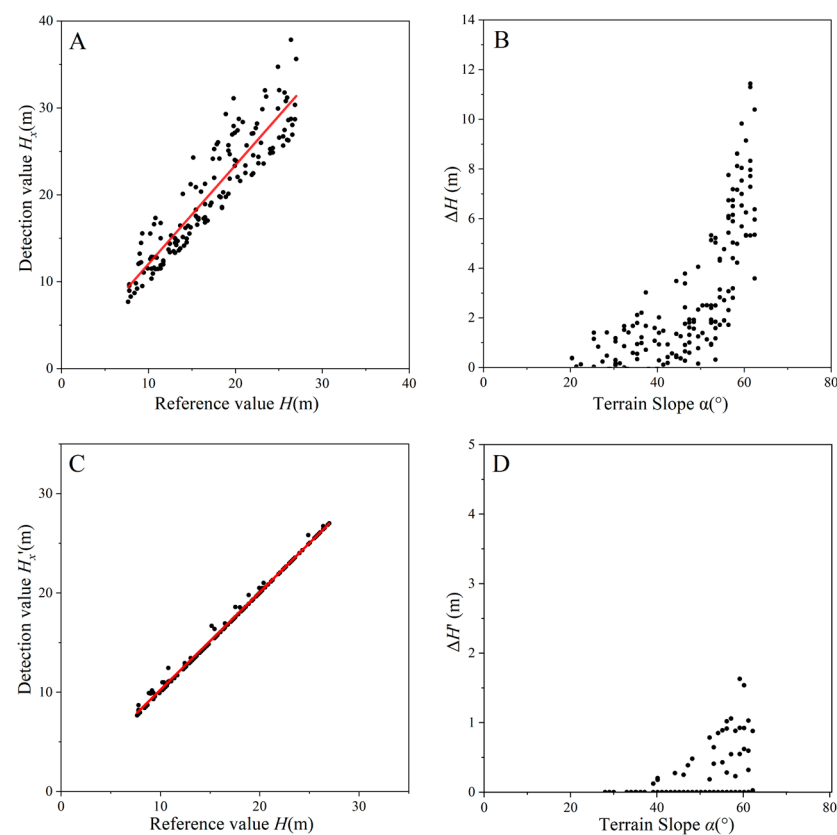


Figure 15. Treetop detection accuracies and influence of the slope gradient on the treetop displacement results. (A,B) show the treetops detected in the CNPC-based NPC, and (C,D) show the treetops detected in the NPCIT-based NPC.

5. Discussion

Evaluating forest carbon reserves based on individual tree heights and the forest canopy height obtained by UAV-LiDAR is considered to be the most convenient, accurate, and reliable technical scheme [41–43]. Many studies have been devoted to individual tree detection methods and tree parameter extraction algorithms, and good progress has been made [44,45]. However, due to the influence of the treetop displacement detected based on the CHM and NPC derived from the topographic normalization of LiDAR point cloud data, the tree parameters extracted by these algorithms may have certain errors. Previously, researchers found that the influence of treetop detection displacements was mainly the result of the crown shape and topographic changes [31–33]. Compared to those studies, in this paper, we have made three major improvements.

(1) In this study, a novel NPC method based on imitated terrain was proposed to effectively attenuate the effect of topographic variations on vegetation-point-cloud normalizations in areas with highly sloping terrain. The NPC was generated by subtracting the elevation of the ground from the original elevation of each feature echo [36]. This method is similar to generating a canopy height model by subtracting a digital elevation model from a DSM [46]. The topographic normalization algorithm is predicated on the assumption that all vegetation is located on locally flat terrain [27], but this assumption is not valid in mountainous forests. Therefore, the original LiDAR point cloud, after topographic normalization, results in the repositioning of all tree point clouds on the plane. At the individual tree scale, the spatial arrangement and position of the trees thus change; at the crown scale, the crown undergoes severe deformation, generating new local maxima (i.e., “false” treetops). This phenomenon, in addition to triggering errors in the treetop displacement and tree height extraction results, was found to significantly alter the vertical extent and curve shape of the plant area index (PAI) profile [17]. The point cloud normalization method based on the NPCIT approach proposed in this study reduced the topographic undulations of the NPC such that crown deformation was not easily generated and the Euclidean distances representing the tree alignment in the NPC were more similar to those in the real scene. This study can help researchers extract tree heights, tree locations, PAIs, etc., from NPC and CHM data.

(2) A physical model with easily accessible parameters was developed in this work to quantify treetop displacements and tree height changes. In the original treetop displacement model, the treetop displacement depends on the slope gradient and the radius of the crown [31]. A theoretical analysis by Alexander et al. [32] showed that the vertical displacement increases exponentially with an increasing slope gradient, regardless of the crown shape or terrain type, thus leading to overestimated individual tree heights. However, those two studies assessed only the effect of topographic normalization on treetop detection in areas with simple terrain and linear slope gradients, and Nie et al. [33] built on this work by exploring the effect of topographic normalization on treetop displacement in areas with more complex and varying terrain types. The crown shape has a significant impact on treetop detection accuracy when using NPCs. For trees with large canopies, the treetop displacements detected from NPCs are obvious [30]. However, the previously considered parameters, such as the crown size, crown shape, and crown angle, are more difficult to obtain. Compared to the parameters required in the original treetop displacement model, all parameters used in our improved treetop displacement model were directly accessible. First, the crown deformation area was obtained using the established algorithm, and false treetops detected after point cloud normalization were identified in the original point cloud. The three-dimensional coordinates of the acquired points were used to directly calculate the horizontal and vertical displacements of the treetops.

(3) We analyzed the horizontal and vertical displacements of detected treetops using an example. Previous studies reported displacements of the treetops detected from NPCs in both the horizontal and vertical directions at the model level but have lacked validations using sample data [32,33]. The main reason for this limitation is that it is more difficult to obtain actual tree measurement data in areas with steep terrain and high slopes than in other areas. In this paper, by conducting a study using UAV-LiDAR data collected in a steep, forested area in the subtropics and performing point cloud normalization based on both the CNPC and NPCIT methods, the horizontal and vertical displacements were calculated using the improved treetop displacement model. An evaluation of the accuracy of the treetop displacement results was carried out by using a manual marking method to record the heights and location attributes of the reference trees. The evaluation results showed that in low-slope terrain, the positions of the detected treetops were similar to the original treetop positions, and basically no displacement occurred. However, in steeply sloping terrain, the displacement values of the detected treetops increased rapidly. Based on this observation, we conclude that the effect of the slope gradient on treetop displacement must be fully considered in extremely steep forested areas.

In addition, although we achieved some improvements in the topographic normalization method and the treetop displacement model in this paper, our methods still have shortcomings. Therefore, we propose the following recommendations for future work. (1) Although the NPCIT method proposed in this study reduces the displacement of the relative positions of trees and detected treetops resulting from terrain changes, irregular stretching still occurs in local areas, and this issue is difficult to control [47]. The required algorithm parameters, such as the starting point and the optimal partition size, also warrant further exploration. (2) Additionally, regarding the crown coverage area of an individual tree, the topography does not completely follow a linear relationship; in practice, high and low undulations occur in forested areas [33]. Therefore, a mathematical treetop displacement model with the ability to adapt to terrain changes needs to be explored. (3) The potential crown volume deformation effect of the proposed method is still unknown. The crown volume is also a commonly used parameter for assessing forest resources, and no crown volume deformation effect has yet been verified [48]. Furthermore, crown volume changes should be studied and added to the theoretical treetop displacement model.

6. Conclusions

In this paper, the treetop detection displacement results for the NPC obtained from LiDAR data collected in an area with steep terrain were verified from modeling, methodological, and case study perspectives. The findings were mainly manifested in the following three aspects.

(1) We proposed a point cloud normalization method based on imitating terrain to reduce the influence of highly sloping terrain on the vertical displacements of tree heights.

(2) We developed a treetop detection displacement model to quantify the treetop displacement and tree height changes without considering the crown shape or crown angle.

(3) We used sample data to verify the influence of the treetop displacement model on the tree height and position detection accuracies.

On the basis of our conclusions, we suggest that with the improvements made to the point cloud data density and quality, it is best to use the treetop displacement model proposed herein to modify extracted tree height parameters, or to use the data containing the original point cloud elevation values to develop an individual tree detection algorithm to minimize the negative impacts of steep terrain on treetop detection results.

Author Contributions: Conceptualization and methodology, H.S. and K.M.; validation, K.M. and F.J.; formal analysis, K.M.; investigation, K.M., F.J., L.X., J.Y., H.H. and H.S.; draft, K.M., C.L. and H.S.; supervision, C.L. and H.S.; review, editing, and revision, K.M., C.L. and H.S.; funding acquisition, K.M., C.L. and H.S. All authors have read and agreed to the published version of the manuscript.

Funding: This research is supported by the Hunan Provincial Natural Science Foundation of China (2020JJ1003 and 2022JJ30078) and the Natural Science Foundation of China (31971578 and 42171418).

Data Availability Statement: Data sharing not applicable.

Conflicts of Interest: The authors declare no conflict of interest.

References

1. Maurizio, S.; Oliver, C.; Johan, E. Dynamics of the Swedish forest carbon pool between 2010 and 2015 estimated from satellite L-band SAR observations. *Remote Sens. Environ.* **2022**, *270*, 112846.
2. Waldeland, A.U.; Øivind, D.T.; Salberg, A. Forest mapping and monitoring in Africa using Sentinel-2 data and deep learning. *Int. J. Appl. Earth Obs. Geoinf.* **2022**, *111*, 102840. [[CrossRef](#)]
3. Katsuto, S.; Tomohiro, N.; Fumiaki, K.; Keiko, F.; Hideki, S. Integrating terrestrial laser scanning and unmanned aerial vehicle photogrammetry to estimate individual tree attributes in managed coniferous forests in Japan. *Int. J. Appl. Earth Obs. Geoinf.* **2022**, *106*, 102658.
4. Hyyppä, J.; Hyyppä, D.; Leckie, F.; Gougeon, X.; Yu, F.; Maltamo, M. Review of methods of small-footprint airborne laser scanning for extracting forest inventory data in boreal forests. *Int. J. Remote Sens.* **2008**, *29*, 1339–1366. [[CrossRef](#)]
5. Abegg, M.; Kükenbrink, D.; Zell, J.; Schaeppman, M.E.; Morsdorf, F. Terrestrial laser scanning for forest inventories—tree diameter distribution and scanner location impact on occlusion. *Forests* **2017**, *8*, 184. [[CrossRef](#)]

6. Persson, H.J.; Olofsson, K.; Holmgren, J. Two-phase forest inventory using very-high-resolution laser scanning. *Remote Sens. Environ.* **2022**, *271*, 112909. [[CrossRef](#)]
7. De Almeida, D.R.A.; Broadbent, E.N.; Ferreira, M.P.; Meli, P.; Maria, A.; Zambrano, A.; Gorgens, E.B.; Resende, A.F.; De Almeida, C.T.; do Amaral, C.H.; et al. Monitoring restored tropical forest diversity and structure through UAV-borne hyperspectral and lidar fusion. *Remote Sens. Environ.* **2021**, *264*, 112582. [[CrossRef](#)]
8. Liu, K.; Wang, A.; Zhang, S.; Zhu, Z.; Bi, Y.; Wang, Y.; Du, X. Tree species diversity mapping using UAS-based digital aerial photogrammetry point clouds and multispectral imageries in a subtropical forest invaded by moso bamboo (*Phyllostachys edulis*). *Int. J. Appl. Earth Obs.* **2021**, *104*, 102587. [[CrossRef](#)]
9. Dong, Z.; Liang, F.; Yang, B.; Xu, Y.; Zang, Y.; Li, J.; Wang, Y.; Dai, W.; Fan, H.; Hyypä, J.; et al. Registration of large-scale terrestrial laser scanner point clouds: A review and benchmark. *ISPRS J. Photogramm. Remote Sens.* **2020**, *163*, 327–342.
10. Vega, C.; Hamrouni, A.; El Mokhtari, S.; Morel, J.; Bock, J.; Renaud, J.P.; Bouvier, M.; Durrieu, S. PTrees: A point-based approach to forest tree extraction from lidar data. *Int. J. Appl. Earth Observ. Geoinf.* **2014**, *33*, 98–108. [[CrossRef](#)]
11. Ma, K.; Chen, Z.; Fu, L.; Tian, W.; Jiang, F.; Yi, J.; Du, Z.; Sun, H. Performance and sensitivity of individual tree segmentation methods for UAV-LiDAR in multiple forest types. *Remote Sens.* **2022**, *14*, 298. [[CrossRef](#)]
12. Liang, X.; Kankare, V.; Hyypä, J.; Wang, Y.; Kukko, A.; Haggrén, H.; Yu, X.; Kaartinen, H.; Jaakkola, A.; Guan, F.; et al. Terrestrial laser scanning in forest inventories. *ISPRS J. Photogramm. Remote Sens.* **2016**, *115*, 63–77. [[CrossRef](#)]
13. Luo, L.; Zhai, Q.; Su, Y.; Ma, Q.; Kelly, M.; Guo, Q. Simple method for direct crown base height estimation of individual conifer trees using airborne LiDAR data. *Opt. Express.* **2018**, *26*, A562–A578. [[CrossRef](#)] [[PubMed](#)]
14. Duncanson, L.I.; Cook, B.D.; Hurtt, G.C.; Dubayah, R.O. An efficient, multi-layered crown delineation algorithm for mapping individual tree structure across multiple ecosystems. *Remote Sens. Environ.* **2014**, *154*, 378–386. [[CrossRef](#)]
15. Fan, L.; Powrie, W.; Smethurst, J.; Atkinson, P.M.; Einstein, H. The Effect of Short Ground Vegetation on Terrestrial Laser Scans at a Local Scale. *ISPRS J. Photogramm. Remote Sens.* **2014**, *95*, 42–52. [[CrossRef](#)]
16. Oshio, H.; Asawa, T.; Hoyano, A.; Miyasaka, S. Estimation of the leaf area density distribution of individual trees using high-resolution and multi-return airborne LiDAR data. *Remote Sens. Environ.* **2015**, *166*, 116–125. [[CrossRef](#)]
17. Liu, J.; Skidmore, A.K.; Heurich, M.; Wang, T. Significant effect of topographic normalization of airborne LiDAR data on the retrieval of plant area index profile in mountainous forests. *ISPRS J. Photogramm. Remote Sens.* **2017**, *132*, 77–87. [[CrossRef](#)]
18. Lu, X.; Guo, Q.; Li, W.; Flanagan, J. A bottom-up approach to segment individual deciduous trees using leaf-off LiDAR point cloud data. *ISPRS J. Photogramm. Remote Sens.* **2014**, *94*, 1–12. [[CrossRef](#)]
19. Marinelli, D.; Paris, C.; Bruzzone, L. A Triangulation-Based Technique for Tree-Top Detection in Heterogeneous Forest Structures Using High Density LiDAR Data. *IEEE Geosci. Remote Sens. Lett.* **2022**, *19*, 1–5. [[CrossRef](#)]
20. Hao, Y.S.; Widagdo, F.R.A.; Liu, X.; Liu, Y.S.; Dong, L.H.; Li, F.G. A Hierarchical Region-Merging Algorithm for 3-D Segmentation of Individual Trees Using UAV-LiDAR Point Clouds. *IEEE Trans. Geosci. Remote Sens.* **2022**, *60*, 1–16. [[CrossRef](#)]
21. Wang, L.; Gong, P.; Biging, G.S. Individual tree-crown delineation and treetop detection in high-spatial-resolution aerial imagery. *Photogramm. Eng. Remote Sens.* **2004**, *70*, 351–357. [[CrossRef](#)]
22. Hu, X.; Chen, W.; Xu, W. Adaptive mean shift-based identification of individual trees using airborne LiDAR data. *Remote Sens.* **2017**, *9*, 148. [[CrossRef](#)]
23. MA, K.; Xiong, Y.; Jiang, F.; Chen, S.; Sun, H. A novel vegetation point cloud density tree-segmentation model for overlapping crowns using UAV LiDAR. *Remote Sens.* **2021**, *13*, 1442. [[CrossRef](#)]
24. Kaartinen, H.; Hyypä, J.; Yu, X.; Vastaranta, M.; Hyypä, H.; Kukko, A.; Holopainen, M.; Heipke, C.; Hirschmugl, M.; Morsdorf, F.; et al. An international comparison of individual tree detection and extraction using airborne laser scanning. *Remote Sens.* **2012**, *4*, 950–974. [[CrossRef](#)]
25. Wang, Y.; Hyypä, J.; Liang, X.; Kaartinen, H.; Yu, X.; Lindberg, E.; Holmgren, J.; Qin, Y.; Mallet, C.; Ferraz, A. International benchmarking of the individual tree detection methods for modeling 3-D canopy structure for silviculture and forest ecology using airborne laser scanning. *IEEE Trans. Geosci. Remote Sens.* **2016**, *54*, 5011–5027. [[CrossRef](#)]
26. Fan, W.; Yang, B.; Dong, Z.; Liang, F.; Xiao, J.; Li, F. Confidence-guided roadside individual tree extraction for ecological benefit estimation. *Int. J. Appl. Earth Obs. Geoinf.* **2021**, *102*, 102368. [[CrossRef](#)]
27. Haala, N.; Brenner, C. Extraction of buildings and trees in urban environments. *ISPRS J. Photogramm. Remote Sens.* **1999**, *54*, 130–137. [[CrossRef](#)]
28. Holmgren, J.; Persson, A. Identifying Species of Individual Trees Using Airborne Laser Scanner. *Remote Sens. Environ.* **2004**, *90*, 415–423. [[CrossRef](#)]
29. VEGA, C.; Durrieu, S. Multi-level filtering segmentation to measure individual tree parameters based on LiDAR data: Application to a mountainous forest with heterogeneous stands. *Int. J. Appl. Earth Obs. Geoinf.* **2011**, *13*, 646–656. [[CrossRef](#)]
30. Duan, Z.; Zhao, D.; Li, Z.; Zhao, Y.; Wu, B.; Zhu, J. Assessing and correcting topographic effects on forest canopy height retrieval using airborne LiDAR data. *Sensors.* **2015**, *15*, 12133–12155. [[CrossRef](#)]
31. Khosravipour, A.; Skidmore, A.K.; Wang, T.; Isenburg, M.; Khoshelham, K. Effect of slope on treetop detection using a LiDAR canopy height model. *ISPRS J. Photogram. Remote Sens.* **2015**, *104*, 44–52. [[CrossRef](#)]
32. Alexander, C.; Korstjens, A.H.; Hill, R.A. Influence of micro-topography and crown characteristics on tree height estimations in tropical forests based on LiDAR canopy height models. *Int. J. Appl. Earth Observ. Geoinf.* **2018**, *65*, 105–113. [[CrossRef](#)]

33. Nie, S.; Wang, C.; Xi, X.H.; Luo, S.Z.; Zhu, X.X.; Li, G.Y.; Liu, H.; Tian, J.Y.; Zhang, S. Assessing the impacts of various factors on treetop detection using LiDAR-derived canopy height models. *IEEE Trans. Geosci. Remote Sens.* **2019**, *57*, 10099–10115. [[CrossRef](#)]
34. RIEGL VUX-1UAV Data Sheet, RIEGL Laser Measurement Systems GmbH, Horn, Austria. 2022. Available online: <http://www.riegl.com/nc/products/airbornescanning/produktdetail/product/scanner/49/> (accessed on 10 March 2023).
35. Silva, V.S.; Silva, C.A.; Mohan, M.; Cardil, A.; Rex, F.E.; Loureiro, G.H.; Almeida, D.R.A.D.; Broadbent, E.N.; Gorgens, E.B.; Dalla, C.A.P.; et al. Combined impact of sample size and modeling approaches for predicting stem volume in eucalyptus spp. forest plantations using field and LiDAR data. *Remote Sens.* **2020**, *12*, 1438. [[CrossRef](#)]
36. Liang, X.; Hyypä, J.; Kaartinen, H.; Lehtomäki, M.; Pyörälä, J.; Pfeifer, N.; Holopainen, M.; Brolly, G.; Francesco, P.; Hackenberg, J.; et al. International benchmarking of terrestrial laser scanning approaches for forest inventories. *ISPRS J. Photogramm. Remote Sens.* **2018**, *144*, 137–179. [[CrossRef](#)]
37. Zhao, X.; Guo, Q.; Su, Y.; Xue, B. Improved progressive TIN densification filtering algorithm for airborne LiDAR data in forested areas. *ISPRS J. Photogramm. Remote Sens.* **2016**, *117*, 79–91. [[CrossRef](#)]
38. Wang, C.; Ji, M.; Wang, J.; Wen, W.; Li, T.; Sun, Y. An improved DBSCAN method for LiDAR data segmentation with automatic Eps estimation. *Sensors* **2019**, *19*, 172. [[CrossRef](#)] [[PubMed](#)]
39. Mohan, M.; Silva, C.; Klauberg, C.; Jat, P.; Catts, G.; Cardil, A.; Hudak, A.T.; Dia, M. Individual tree detection from unmanned aerial vehicle (UAV) derived canopy height model in an open canopy mixed conifer forest. *Forests* **2017**, *8*, 340. [[CrossRef](#)]
40. Kutner, M.H.; Nachtsheim, C.J.; Neter, J.; Wasserman, W. Linear regression with one predictor variable. In *Applied Linear Statistical Models*, 5th ed.; McGraw-Hill/Irwin: Chicago, IL, USA, 2004; Volume 1, pp. 1–5.
41. Dai, W.; Yang, B.; Dong, Z.; Shaker, A. A new method for 3D individual tree extraction using multispectral airborne LiDAR point clouds. *ISPRS J. Photogram. Remote Sens.* **2018**, *144*, 400–411. [[CrossRef](#)]
42. López Serrano, F.R.; Rubio, E.; García Morote, F.A.; Andrés Abellán, M.; Picazo Córdoba, M.I.; García Saucedo, F.; Martínez García, E.; Sánchez García, J.M.; Serena Innerarity, J.; Carrasco Lucas, L.; et al. Artificial intelligence-based software (AID-FOREST) for tree detection: A new framework for fast and accurate forest inventorying using LiDAR point clouds. *Int. J. Appl. Earth Obs. Geoinf.* **2022**, *113*, 103014. [[CrossRef](#)]
43. Han, X.; Dong, Z.; Yang, B. A point-based deep learning network for semantic segmentation of MLS point clouds. *ISPRS J. Photogram. Remote Sens.* **2021**, *175*, 199–214. [[CrossRef](#)]
44. Liang, X.; Wang, Y.; Pyörälä, J.; Lehtomäki, M.; Yu, X.; Kaartinen, H.; Kukko, A.; Honkavaara, E.; Issaoui, A.E.I.; Nevalainen, O.; et al. Forest in situ observations using unmanned aerial vehicle as an alternative of terrestrial measurements. *For. Ecosyst.* **2019**, *6*, 1–16. [[CrossRef](#)]
45. Mengesha, T.; Hawkins, M.; Nieuwenhuis, M. Validation of terrestrial laser scanning data using conventional forest inventory methods. *Eur. J. Forest Res.* **2015**, *134*, 211–222. [[CrossRef](#)]
46. Khosravipour, A.; Skidmore, A.; Isenburg, M.; Wang, T.; Hussin, Y. Generating Pit-free Canopy Height Models from Airborne Lidar. *Photogramm. Eng. Remote Sens.* **2014**, *80*, 863–872. [[CrossRef](#)]
47. Chen, Q.; Wang, H.; Zhang, H.; Sun, M.; Liu, X. A point cloud filtering approach to generating DTMs for steep mountainous areas and adjacent residential areas. *Remote Sens.* **2016**, *8*, 71. [[CrossRef](#)]
48. Kükenbrink, D.; Schneider, F.D.; Leiterer, R.; Schaepman, M.E.; Morsdorf, F. Quantification of hidden canopy volume of airborne laser scanning data using a voxel traversal algorithm. *Remote Sens. Environ.* **2017**, *194*, 424–436. [[CrossRef](#)]

Disclaimer/Publisher’s Note: The statements, opinions and data contained in all publications are solely those of the individual author(s) and contributor(s) and not of MDPI and/or the editor(s). MDPI and/or the editor(s) disclaim responsibility for any injury to people or property resulting from any ideas, methods, instructions or products referred to in the content.